ACCSCIENCE PUBLISHING

Journal of Seismic Exploration

ARTICLE

Multi-level facies-constrained reservoir prediction and application in a sparse-well area of the Qiongdongnan Basin

Wanyuan Sun*, Shiyou Liu, Rui Wang, and Shuxian Liu

Research Institute, China National Offshore Oil Corporation Hainan branch, Haikou, Hainan, China

Abstract

The deepwater area of the Qiongdongnan Basin is characterized by sparse well control, low-porosity, and low-permeability reservoirs, weak seismic responses, and small elastic-parameter contrasts. These conditions increase the non-uniqueness of conventional reservoir prediction. To reduce this uncertainty, this study proposes a multi-level facies-constrained reservoir prediction workflow that couples sedimentary facies, seismic facies, and logging lithofacies. The workflow first constructs a facies prior from seismic waveform classification, well-log interpretation, and sedimentary constraints. It then performs Bayesian pre-stack inversion based on the exact Zoeppritz equation, followed by semi-supervised porosity prediction and frequency-dependent amplitude variation with offset flowability analysis. Finally, the P/S velocity ratio, porosity, and water-saturation-related attributes are integrated using a competitive neural network to delineate favorable reservoir zones. Synthetic tests and a Stanford reservoir model test show that the proposed method improves facies agreement from 78.57% to 92.86% relative to a conventional facies-constrained workflow. Because the field area contains only one drilled well, the field results are interpreted as probabilistic exploration targets rather than blind-well proof of deterministic accuracy. The workflow provides a reproducible and geologically constrained approach for reservoir prediction in sparse-well deepwater settings.

Keywords: Reservoir prediction; Facies-constrained inversion; Competitive neural network; Sparse-well area; Qiongdongnan Basin

***Corresponding author:**
Wanyuan Sun
(sunwy5@cnooc.com.cn)

Citation: Sun W, Liu S, Wang R, Liu S. Multi-level facies-constrained reservoir prediction and application in a sparse-well area of the Qiongdongnan Basin. *J Seismic Explor*.
doi: 10.36922/JSE026210087

Received: May 19, 2026

Revised: July 30, 2026

Accepted: August 5, 2026

Published online: November 16, 2026

Copyright: © 2026 Author(s). This is an Open-Access article distributed under the terms of the Creative Commons Attribution License, permitting distribution, and reproduction in any medium, provided the original work is properly cited.

Publisher's Note: AccScience Publishing remains neutral with regard to jurisdictional claims in published maps and institutional affiliations.

1. Introduction

The Qiongdongnan Basin is one of the most important deepwater natural gas provinces in the northern South China Sea. In the northern slope of the Baodao Sag, reservoir prediction is difficult because drilling control is sparse, target sand bodies are deeply buried, reservoir quality is heterogeneous, and the contrast in elastic parameters between reservoir and non-reservoir intervals is weak. Conventional inversion and attribute-analysis workflows commonly depend on dense well calibration and may produce non-unique solutions in such settings. Facies-constrained inversion reduces this non-uniqueness by using sedimentary facies, seismic facies, and lithofacies as geological priors rather than relying only on seismic amplitudes or a single well model.[1-8]

International scholars have conducted extensive pioneering and systematic

research on facies-constrained inversion, establishing a comprehensive theoretical system and methodological framework for this technology. Scholars such as Caers[9] have driven a core technological leap in facies-constrained inversion from two-point to multi-point statistics.[9,10] At the same time, Bosch *et al.*[11] have systematically developed a joint inversion framework that integrates geostatistics and statistical petrophysical models, thereby refining the theoretical petrophysical foundation of facies-constrained inversion. Regarding inversion solution methods, Buland and Omre[12] established the classic Bayesian linearized amplitude variation with offset (AVO) inversion framework, while Chen[13], Larsen *et al.*[14], and others further developed the nonlinear inversion method for the exact Zoeppritz equation under phase constraints. This approach significantly improved computational efficiency while maintaining inversion accuracy, thereby driving the evolution of facies-constrained inversion from post-stack impedance inversion to pre-stack full-waveform elastic-parameter inversion.[13,14] In recent years, artificial intelligence technologies have opened new avenues for facies-constrained reservoir prediction. Liu *et al.*[15] combined deep convolutional neural networks with generative adversarial networks to construct a supervised-semi-supervised fusion phase classification method, effectively improving the accuracy and efficiency of seismic facies identification; the pre-stack texture-constrained semi-supervised seismic phase analysis method proposed by Cai *et al.*[16] further achieved dual improvements in microfacies identification accuracy and lateral resolution. Regarding multi-attribute fusion in seismic data, Zhao *et al.*[17] proposed a multi-attribute automatic fusion method based on fast independent component analysis, which effectively removes correlations among features captured by higher-order statistics. For reservoir prediction in low-well-count areas, Song *et al.*[18] demonstrated that semi-supervised neural networks perform better in avoiding overfitting and are more suitable for low-well-count conditions during exploration or early development stages. Dhara *et al.*[19] introduced machine learning-assisted prior information into a cross-dimensional Bayesian inversion framework, enabling joint inversion of lithofacies and elastic parameters and thereby further expanding the depth of application of artificial intelligence technology in facies-constrained inversion.

Meanwhile, local scholars have made a series of significant advancements in the localization and engineering application of facies-constrained inversion technology, tailored to the unique geological conditions of China's terrestrial basins and the deepwater basins of the South China Sea. Xie *et al.*[20,21] systematically summarized the innovative achievements in oil and gas accumulation theory and technology in the deepwater areas of the northern South China Sea, establishing a series of key technologies for deepwater oil and gas exploration that encompass geophysical exploration, reservoir prediction, and safe drilling and completion. Building on this foundation, the researchers further proposed a facies-constrained reservoir prediction method based on seismic configuration, which effectively improved reservoir prediction accuracy in deepwater areas with sparse well networks through the combined constraints of topographic and lithologic phases[22], and developed a strategy for virtual well construction and deepwater canyon facies-constrained modeling based on sedimentary simulation, providing a new technical pathway for reservoir characterization under sparse well network conditions.[23] Yin *et al.*[24] introduced intelligent optimization algorithms into the pre-stack inversion framework, developing a pre-stack stochastic inversion method based on a hybrid genetic algorithm and a pre-stack AVO inversion technique based on a differential evolution algorithm[25], thereby achieving the effective integration of facies-constrained pre-stack inversion with intelligent optimization algorithms. Regarding reservoir prediction in the deepwater areas of the South China Sea, Liang *et al.*[26] applied diagenetic facies analysis to reservoir prediction in the deepwater areas of the Baiyun Basin, establishing a causal relationship between diagenetic facies and pore evolution, and providing a new technical approach for predicting favorable reservoirs in deepwater areas with sparse well networks. Furthermore, to address the challenge of identifying hidden reservoirs with minimal variations in elastic parameters, Yin *et al.*[27] proposed a high-resolution inversion method driven by waveforms and constrained by multiple parameters. By using variations in seismic waveforms to infer lithofacies composition, they achieved high-precision reservoir-parameter inversion within a Bayesian framework.[27,28] These research findings have effectively supported the exploration and discovery of multiple deepwater gas fields in China's South China Sea, providing crucial technical support for reservoir prediction in deepwater areas with sparse well networks. However, existing facies-constrained inversion techniques still face three major bottlenecks in practical applications. First, conventional methods are highly dependent on the quantity and spatial distribution of well data. Under single-well or sparse-well-network conditions, it is difficult to construct high-precision initial models and effective constraints, leading to significant multivaluedness in inversion results. This results in a marked decline in prediction accuracy, particularly in highly heterogeneous reservoirs. Second, the integration of multi-source facies information remains insufficient. Existing methods often rely on single-facies constraints or linearly weighted

fusion, making it difficult to characterize the nonlinear relationships among seismic facies, sedimentary facies, lithofacies, and reservoir elastic parameters. Consequently, their ability to identify lithofacies and distinguish fluids is limited for concealed reservoirs with small variations in elastic parameters. Furthermore, the current technical framework lacks sufficient integration. It has not yet established a comprehensive workflow spanning "intelligent fusion of facies information—high-precision facies-controlled inversion—quantitative prediction of physical properties—gas content detection—and comprehensive sweet spot evaluation," making it difficult to meet the practical engineering demands of exploration and development in deepwater areas with sparse well coverage.

To address these issues, this study focuses on the northern slope of the Baodao Sag in the Qiongdongnan Basin and investigates reservoir prediction under sparse-well conditions. The novelty of the work lies in the integration of four linked steps: (i) probabilistic coupling of sedimentary facies, seismic waveform facies, and logging lithofacies; (ii) Bayesian pre-stack inversion based on the exact Zoeppritz equation using the coupled facies model as a prior; (iii) semi-supervised porosity prediction that uses the limited labeled well samples and unlabeled seismic samples simultaneously; and (iii) competitive neural network fusion of P/S velocity ratio, porosity, and water-saturation related attributes for sweet-spot ranking. The individual methods are not claimed as entirely new; the contribution is the internally consistent, facies-constrained workflow designed for sparse-well deepwater exploration.

2. Methodology

2.1. Geological background and response mechanism analysis of the study area

The study area is located on the northern slope of the Baodao Sag in the Qiongdongnan Basin, northwestern South China Sea.[29-31] Figure 1 shows core photographs from Well A1 in the target interval. The target interval is the third member of the Lingshui Formation. The available calibration data include Well A1, core observations at 3,861 m, 3,864 m, and 3,896 m, conventional well logs, interpreted lithofacies, and a three-dimensional (3D) pre-stack seismic dataset. The target interval contains four mapped sand bodies, namely 3U-A, 3U-B, 3L-A, and 3L-B. Because only one drilled well is available in the study area, no blind field well can be used for independent validation. Therefore, reliability was evaluated using synthetic tests, a 3D Stanford reservoir model with pseudo-wells, consistency with the A1 core-log interpretation, and geological consistency with the sedimentary model. The field prediction should be regarded as a probabilistic sweet-spot ranking for exploration deployment. The key data items and their respective validation roles are summarized in Table 1.

2.2. Technical approach

The technical workflow followed a facies-constrained logic rather than a simple stacking of independent methods. Sedimentary facies were interpreted from regional depositional knowledge, core observations, and well-log response. Seismic facies were extracted from waveform and pre-stack attribute patterns. Logging lithofacies were interpreted from Well A1 and used to anchor the geological meaning of seismic clusters. These three facies types were coupled through probabilistic calibration: each seismic waveform cluster was assigned a sedimentary-facies probability and a lithofacies probability, and the coupled probability volume was used as the prior constraint for inversion and later attribute fusion.

Sedimentary-facies constraints were built from sequence stratigraphy, core observations, and log-

Table 1. Field data and validation constraints used in this study

Data item	Use in workflow	Validation role
Well A1 logs and core	Lithofacies interpretation, porosity calibration, facies mapping	Calibration and well-tie check
3D pre-stack seismic angle gathers	Exact-Zoeppritz PP inversion and frequency-dependent AVO analysis	Field application input
Sedimentary facies model	Geological prior for facies transition and sand-body continuity	Geological plausibility check
Single-well synthetic model	Noise-resistance test with a 30 Hz Ricker wavelet and SNR = 4	Algorithm stability test
Stanford reservoir model	Pseudo-well and plane-slice comparison	Independent model-space verification

Abbreviations: AVO: Amplitude variation with offset; PP: P-wave–P-wave; SNR: Signal-to-noise ratio.

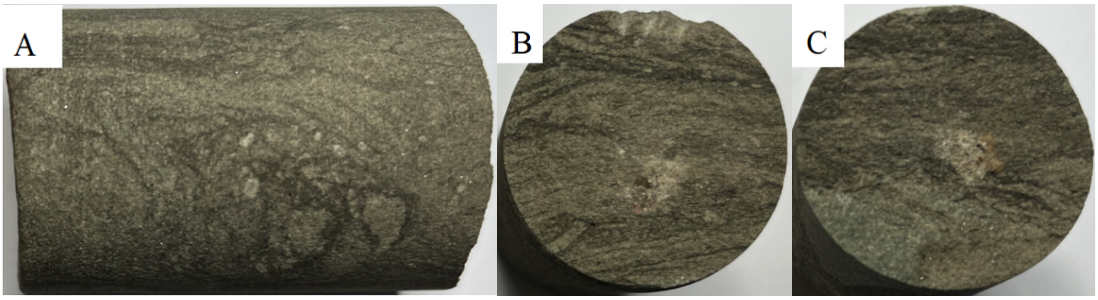


Figure 1. Well A1 Lingshui Formation three-stage core log photographs. (A) 3,861 m, gray muddy siltstone with well-developed muddy bands; (B) 3,864 m, gray muddy siltstone with low-angle cross-bedding; (C) 3,896 m, gray muddy siltstone with well-developed muddy bands.

interpreted lithofacies. Seismic waveform facies were classified and calibrated to sedimentary facies using Well A1 and stratigraphic surfaces. A coupled facies-prior model was constructed by integrating seismic facies, sedimentary facies, and logging lithofacies with a competitive neural network. Bayesian pre-stack inversion was performed with the exact Zoeppritz equation, using the coupled facies model as a prior constraint. Porosity was predicted using semi-supervised deep learning, and gas-related anomalies were detected using frequency-dependent AVO and relative flowability attributes. The P/S velocity ratio, porosity, and water-saturation-related attributes were fused to classify Class I favorable zones, Class II favorable zones, and non-favorable zones. The complete workflow is illustrated in Figure 2.

2.3. Multi-level facies fusion

Facies fusion was performed in two steps. First, sensitive log and seismic attributes were normalized and reduced using principal component analysis (PCA) to suppress redundant information. Second, fuzzy C-means (FCM), self-organizing map (SOM), and competitive neural network clustering were compared using the A1 lithofacies interpretation as calibration. The number of clusters was fixed at four according to the lithofacies scheme: sandstone with good properties, sandstone with moderate properties, sandstone with poor properties, and shale.

Figure 3 compares the lithofacies clustering results of the three methods at Well A1. The comparison shows that FCM, SOM, and the competitive neural network achieved lithofacies agreement rates of 71.4%, 80.3%, and 86.6%, respectively, at the calibration well. The competitive neural network was therefore selected for facies fusion. Because these values were derived from the single calibration well, they were used only to rank methods and not to claim blind-field accuracy.

A competitive neural network is an unsupervised clustering model in which neurons compete for each input vector, and only the winning neuron and its neighborhood update their weights.[32,33] In this study, the input layer comprised normalized sensitive attributes, the competitive layer comprised four neurons corresponding to the four lithofacies classes, and the output layer was mapped to geological facies using Well A1. Euclidean distance was used as the competition criterion. The learning rate decayed from 0.10 to 0.01, the maximum number of iterations was 500, and convergence was reached when the change in the weight matrix was less than 1.0×10^{-4} or when the maximum iteration number was reached.

The selected sensitive attributes x were first standardized to [0, 1] to remove differences in units and magnitude. The facies-fusion calculation therefore followed a reproducible sequence: attribute screening, normalization, PCA reduction, four-class competitive clustering, calibration of cluster identities at Well A1, conversion of cluster distance to probability, and construction of the 3D facies-prior volume. The four-class definition, learning-rate schedule, stopping criterion, and maximum iteration number are kept identical for all target intervals.

$$x_{i'} = \frac{x_i - \min(x_i)}{\max(x_i) - \min(x_i)} \tag{1}$$

where i represents the sample. PCA was then used to obtain orthogonal components from the standardized attributes and to suppress redundant information. The eigenvalue equation is given as **Equation 2**:

$$Rq_j = \lambda_j q_j \tag{2}$$

where R is the covariance matrix of the standardized input attributes, q_j is the j eigenvector, and λ_j is the corresponding eigenvalue. The cumulative contribution rate is shown as **Equation 3**:

$$C_p = \frac{\sum_{j=1}^{p} \lambda_j}{\sum_{j=1}^{m} \lambda_j} \tag{3}$$

Principal components with a cumulative contribution rate greater than the selected threshold were retained as

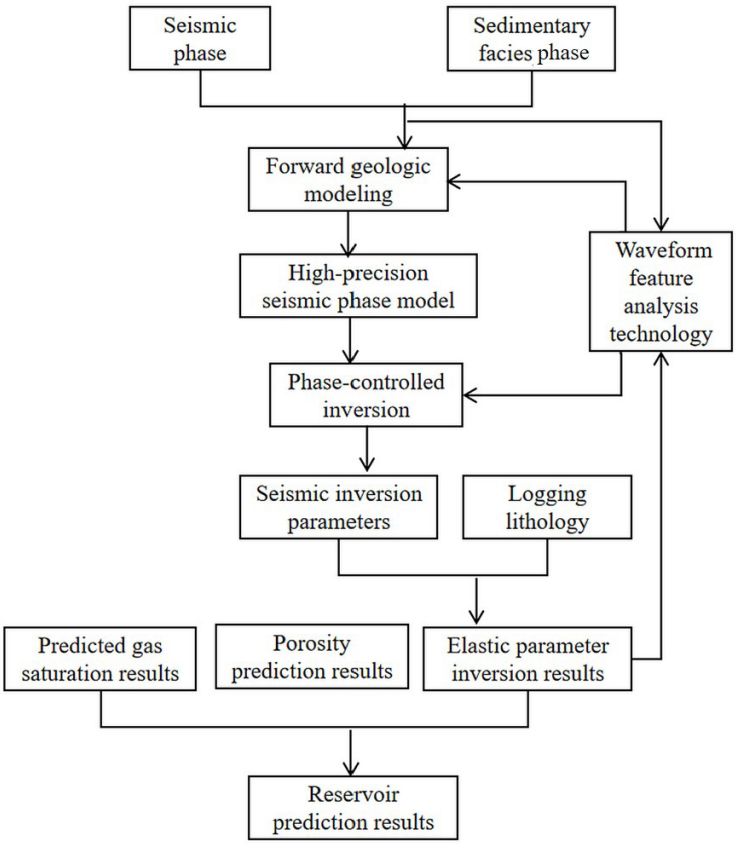


Figure 2. Workflow of the multi-level facies-constrained reservoir prediction method, including facies-prior construction, exact Zoeppritz inversion, porosity prediction, gas-sensitive attribute extraction, and sweet-spot classification

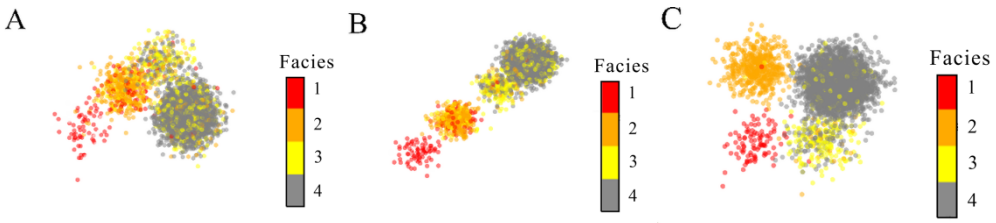


Figure 3. Lithofacies clustering results at Well A1. (A) Fuzzy C-means clustering. (B) Self-organizing map clustering. (C) Competitive neural network clustering. Colors denote the four log-interpreted lithofacies classes; higher separation indicates lower lithofacies overlap.

the input set S. For class C_i, the competitive neuron has a weight vector $\mathbf{W}_i$. The Kohonen update rule is given as **Equation 4**:

$$\boldsymbol{W}_i(t+1)=\boldsymbol{W}_i(t)+\alpha(t)\left[\boldsymbol{s}(t)-\boldsymbol{W}_i(t)\right] \tag{4}$$

where $\alpha(t)$ is a time-decaying learning rate and $s(t)$ is the retained principal-component vector. The winning neuron is the class whose weight vector has the minimum Euclidean distance from the input vector. The output mapping is shown as **Equation 5**:

$$C_i = argmin_i \left\|\boldsymbol{s}-\boldsymbol{W}_i\right\|_2 \tag{5}$$

To convert the clustering result into a geological probability volume, the distance-based cluster score was mapped to [0, 1] using a sigmoid function (**Equation 6**):

$$P_f = \frac{1}{1+\exp(-z_i)} \tag{6}$$

In this formulation, P_f is the favorable-facies probability, and z_i is the normalized score of cluster i. The coupled seismic-sedimentary-lithofacies probability volume

was then used to build the initial facies-prior model for inversion. This coupling is probabilistic rather than a one-to-one deterministic assignment, which is important under single-well conditions.

Based on well-logging facies data, combined with results from automatic seismic facies recognition and sedimentary patterns, the initial facies model for the Baodao North Slope basin was established. Initial facies model slices were extracted from the 3U-A, 3U-B, 3L-A, and 3L-B sand-body layers, as shown in Figure 4. The facies slice results demonstrate that the constructed initial facies model clearly reflects the sedimentary characteristics of the sand bodies and provides a preliminary characterization of the planar distribution patterns of multi-level sand bodies. The initial facies model obtained from this modeling served as the data foundation for the first round of facies-controlled inversion.

2.4. Bayesian exact Zoeppritz inversion under facies constraints

The inversion used the exact Zoeppritz equation within a Bayesian framework. Only PP-wave pre-stack angle gathers were available for the field dataset; consequently, the field objective function contains a PP residual and a facies-conditioned model-prior term, but no PS residual. The joint PP–PS expression was provided only as a general extension for datasets that included reliable converted-wave observations.

The P/S velocity ratio is sensitive to lithology and fluid effects and was therefore used as the main elastic attribute for subsequent reservoir prediction. The facies-prior model constrains lateral continuity, while the Bayesian term stabilizes inversion under sparse well control.

Let $\mathbf{d}_{obs}$ denote the observed PP-wave pre-stack seismic data, $\mathbf{m} = [V_p, V_s, \rho]^T$ denote the model vector, $\mathbf{G}_m$ denote the exact Zoeppritz forward operator, $\mathbf{J}$ denote the Jacobian matrix evaluated at the current model, f denote the facies, $\mathbf{C}_d$ denote the data-error covariance, and $\mathbf{C}_m$ denote the model-prior covariance. Linearization around $\mathbf{m}_k$ gives **Equation 7**:

$$\boldsymbol{G}(\boldsymbol{m}_k + \delta\boldsymbol{m}) \cong \boldsymbol{G}(\boldsymbol{m}_k) + \boldsymbol{J}_k \delta\boldsymbol{m} \tag{7}$$

The PP-wave Bayesian objective function is given as **Equation 8**:

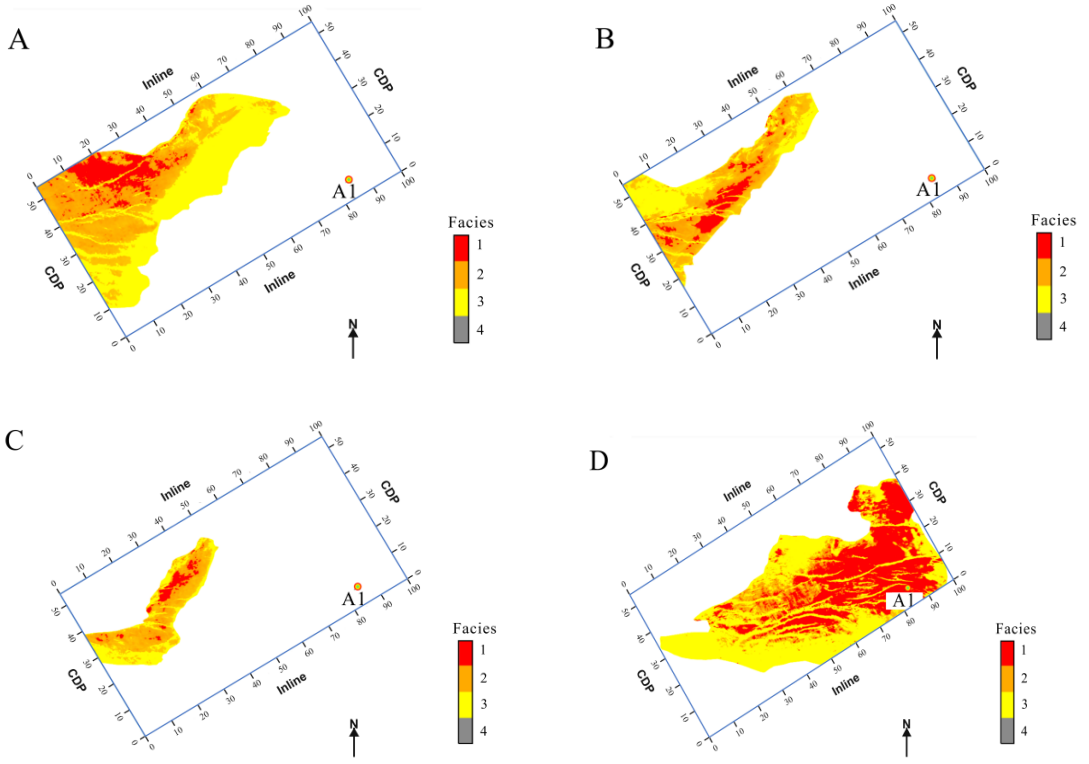


Figure 4. Initial facies-prior model for the four sand bodies. (A) 3U-A. (B) 3L-A. (C) 3U-B. (D) 3L-B. The slices show the spatial distribution of coupled seismic facies, sedimentary facies, and logging lithofacies probabilities.

$$\Phi(\delta \boldsymbol{m}) = \boldsymbol{C}_d^{-1/2}\left[\boldsymbol{d}_{\text{obs}} - \boldsymbol{G}(\boldsymbol{m}_k) - \boldsymbol{J}_k \delta \boldsymbol{m}\right]_2^2 + \lambda^2 \boldsymbol{C}_m^{-1/2}\left(\boldsymbol{m}_k + \delta \boldsymbol{m} - \boldsymbol{m}_{\text{prior}}\right)_2^2 + \beta \boldsymbol{W} \delta \boldsymbol{m}_1 \quad (8)$$

$$\boldsymbol{m}_{\text{prior}} = E\left[\boldsymbol{m} \mid f\right], \quad \boldsymbol{C}_m = \text{cov}[\boldsymbol{m} \mid f] \quad (9)$$

Taking the derivative of Φ with respect to δ_m and setting it to zero gives the normal **Equation 10**:

$$\left[\boldsymbol{J}_k^T \boldsymbol{C}_d^{-1} \boldsymbol{J}_k + \lambda^2 \boldsymbol{C}_m^{-1} + \beta \boldsymbol{W}^T \boldsymbol{W}\right] \delta \boldsymbol{m} = \boldsymbol{J}_k^T \boldsymbol{C}_d^{-1}\left[\boldsymbol{d}_{\text{obs}} - \boldsymbol{G}(\boldsymbol{m}_k)\right] - \lambda^2 \boldsymbol{C}_m^{-1}\left(\boldsymbol{m}_k - \boldsymbol{m}_{\text{prior}}\right) \quad (10)$$

The model perturbation was solved iteratively by an iterative reweighted least-squares scheme (**Equation 11**):

$$\delta \boldsymbol{m}_k = \boldsymbol{H}_k^{-1} \boldsymbol{g}_k \quad (11)$$

The model update is shown as **Equation 12**:

$$\boldsymbol{m}_{k+1} = \boldsymbol{m}_k + \eta_k \delta \boldsymbol{m}_k \quad (12)$$

where n_k is the step-size factor, $\mathbf{H}_k$ is the approximate Hessian matrix in **Equation 10**, and $\mathbf{g}_k$ is the right-hand-side gradient vector. Iteration stopped when the relative data-misfit reduction or the relative model update was less than 1×10^{-3}, or when the maximum iteration number was reached.

If converted-wave data were available, the objective function was extended to a joint PP–PS inversion (**Equation 13**):

$$\Phi_{\text{joint}} = \Phi_{\text{PP}} + \gamma \boldsymbol{C}_{\text{PS}}^{-1/2}\left[\boldsymbol{d}_{\text{PS}} - \boldsymbol{G}_{\text{PS}}(\boldsymbol{m})\right]_2^2 \quad (13)$$

where γ is the relative weight of the PS-wave residual. This optional term was not used in the field application because no reliable PS-wave seismic volume was available (**Equation 14**):

$$\boldsymbol{J}_k = \left.\frac{\partial \boldsymbol{G}(\boldsymbol{m})}{\partial \boldsymbol{m}}\right|_{\boldsymbol{m}=\boldsymbol{m}_k} \quad (14)$$

Second-order derivatives were not explicitly calculated in the practical inversion because they substantially increase computational cost and are unstable under noisy sparse-well conditions.

$$\boldsymbol{H}_k \approx \boldsymbol{J}_k^T \boldsymbol{C}_d^{-1} \boldsymbol{J}_k + \lambda^2 \boldsymbol{C}_m^{-1} + \beta \boldsymbol{W}^T \boldsymbol{W} \quad (15)$$

The simplified Hessian in **Equation 15** provides a stable compromise between nonlinear accuracy and computational efficiency.

$$\delta \boldsymbol{m}_k = \boldsymbol{H}_k^{-1} \boldsymbol{g}_k \quad (16)$$

This formulation gives a readable and reproducible inversion workflow: the facies prior defines $\mathbf{m}_{\text{prior}}$ and $\mathbf{C}_m$, the exact Zoeppritz operator computes the PP reflection response, and iteratively reweighted least squares reduces the influence of outliers and preserves weak reservoir reflections.

Figure 5 illustrates the initial-model construction process. The conventional interpolation model was biased because it depended mainly on stratigraphic and well interpolation. The waveform-constrained model improved lateral continuity but still lacked explicit sedimentary meaning. The coupled facies-prior model integrated seismic waveform facies, sedimentary facies, and log-interpreted lithofacies, and therefore better represents structural details and multi-level sand-body distribution.

Figure 6 compares planar attribute slices from different initial-modeling methods. The facies-constrained model in Figure 6B locally matched the seismic-facies pattern well, whereas the multi-level facies-constrained models in Figure 6C and 6D provided a more continuous and geologically interpretable sand-body framework. Accordingly, the comparison was based on continuity, geological plausibility, and agreement with the available calibration data rather than on an assumption that one model is uniformly superior in every local area.

The P/S velocity-ratio slices in Figure 7 were extracted from the facies-constrained inversion results. Low P/S velocity-ratio anomalies are interpreted as relatively favorable reservoir-fluid responses only when they are spatially consistent with sedimentary facies, porosity, and gas-sensitive attributes. This multi-attribute consistency check was used to reduce false anomalies caused by noise or local tuning effects.

3. Synthetic and model validation before field application

Before applying the workflow to the field data, two validation tests were conducted. First, a single-well synthetic model was built from the A1 log trend. The exact Zoeppritz reflection coefficients were calculated from the true model and convolved with a 30 Hz Ricker wavelet. Random noise with a root-mean-square signal-to-noise ratio of 4 was added to test stability. Figure 8 shows the single-well synthetic model. Second, the Stanford reservoir model was used as an independent 3D model test with 14 pseudo-wells. Figure 9 compares the synthetic inversion results of the multi-level facies-constrained method and the conventional method. These tests evaluate algorithmic stability and facies agreement, but they are not a substitute for blind field-well validation.

The Stanford reservoir model was used to test the method under a 3D multi-sand-body setting similar to the stacked sand bodies in the third member of the Lingshui Formation (Figure 10). Compared with the conventional facies-constrained inversion, the proposed workflow better preserves sand-body boundaries and internal morphology in the model test. This result supports the use of coupled

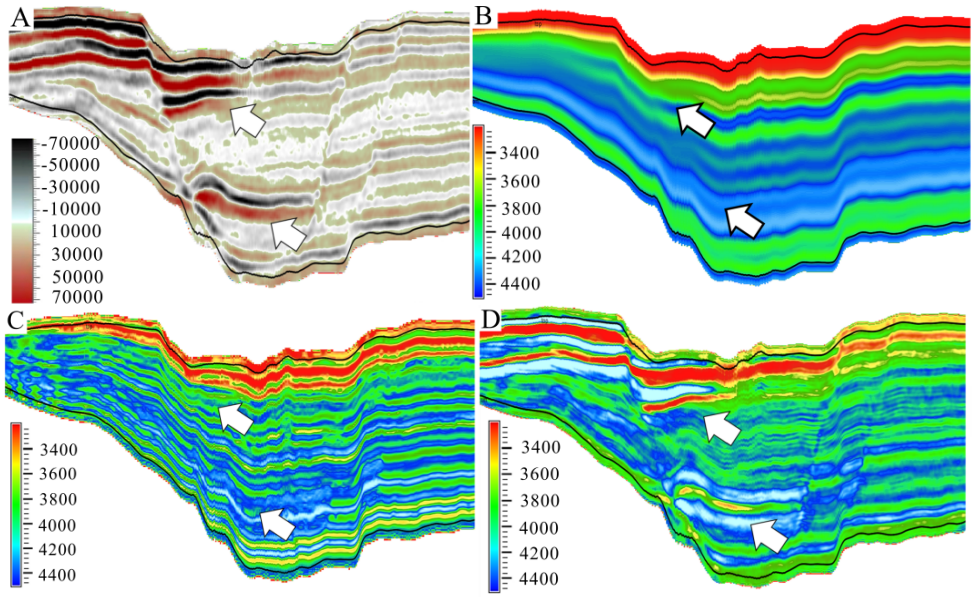


Figure 5. Comparison of initial models. (A) Actual seismic profile. (B) Conventional interpolation model. (C) Initial model constrained by a single seismic-facies cluster from waveform classification. (D) Initial model constrained by coupled multi-facies simulation.

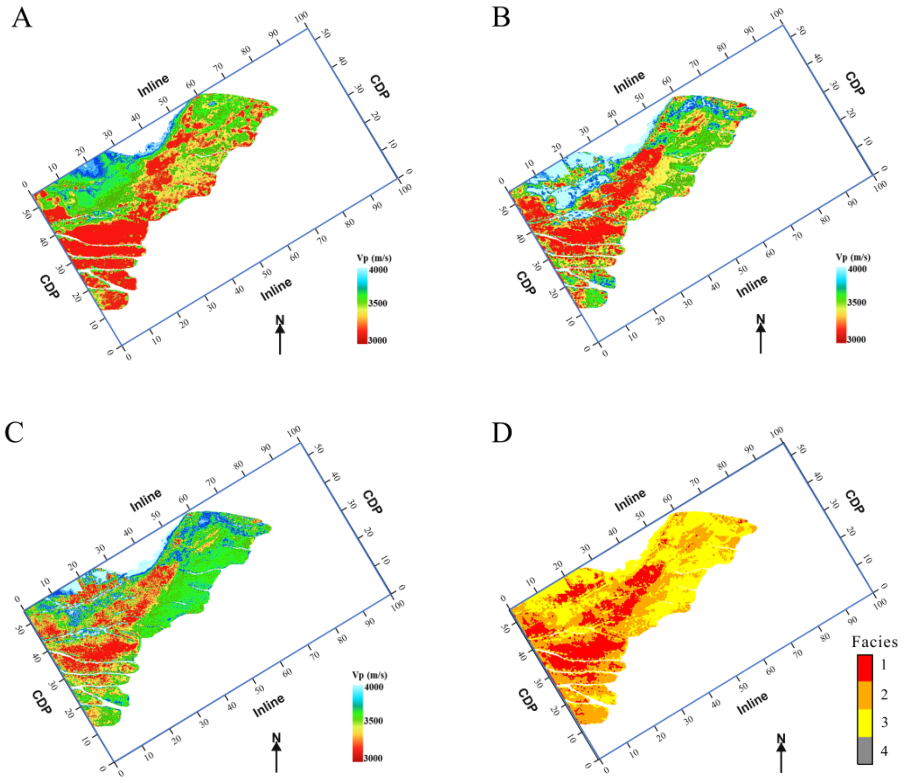


Figure 6. Planar attribute slices from different initial-modeling methods. (A) Conventional interpolation model. (B) Seismic-facies constrained model. (C) Multi-level facies-constrained simulation model. (D) Coupled multi-facies geological model.

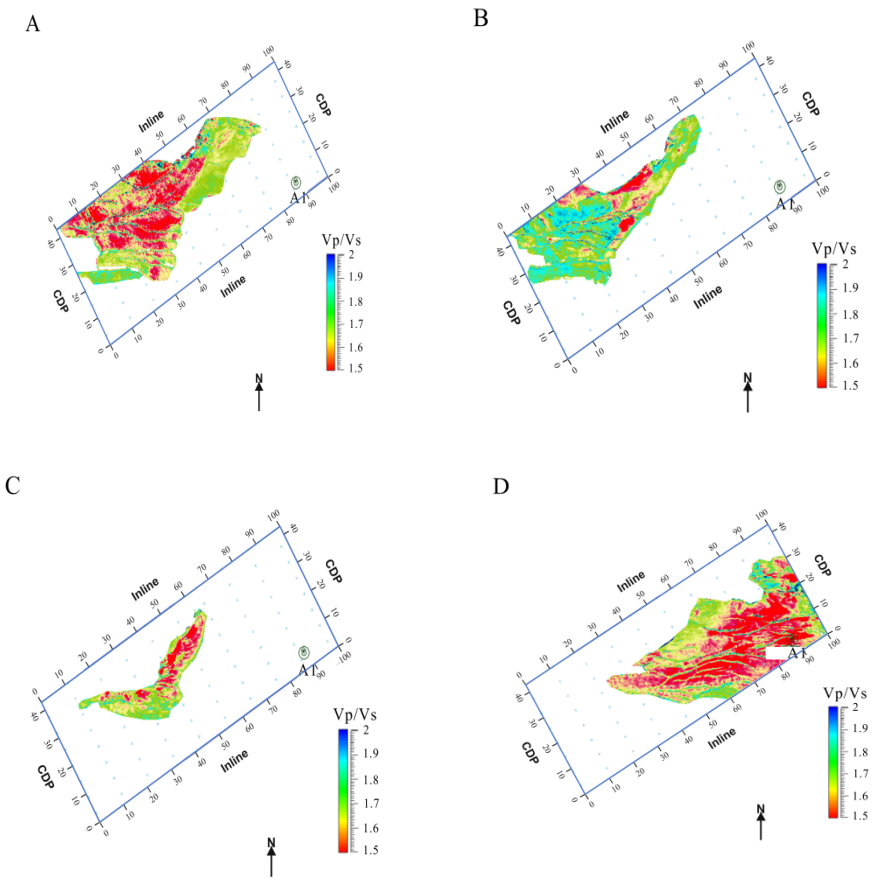


Figure 7. Planar slices of the P/S velocity ratio for the target sand bodies. (A) 3U-A. (B) 3L-A. (C) 3U-B. (D) 3L-B. Lower values indicate relatively stronger reservoir-fluid sensitivity under the local rock-physics calibration.

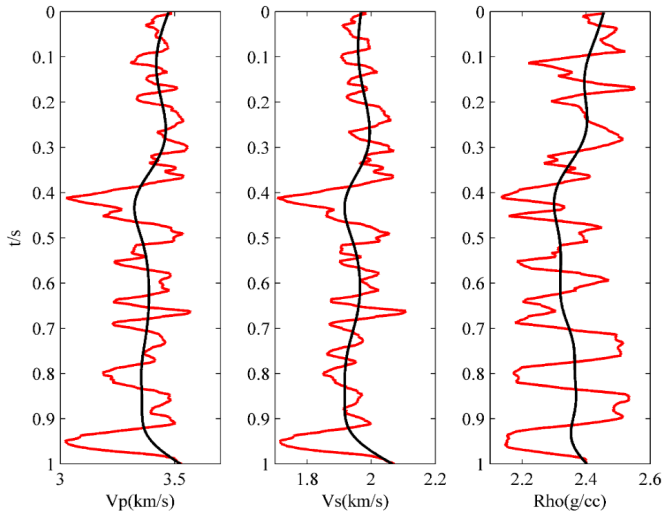


Figure 8. Single-well synthetic model. The red curve denotes the target model, and the black curve denotes the initial model.

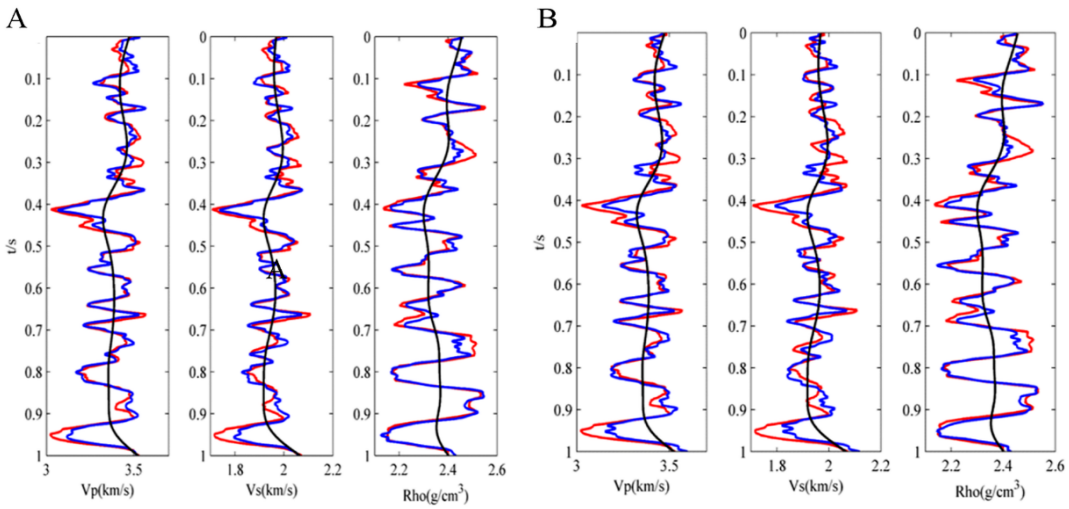


Figure 9. Synthetic inversion comparison. (A) Multi-level facies-constrained inversion. (B) Conventional facies-constrained inversion. The test used a 30 Hz Ricker wavelet and a signal-to-noise ratio of 4 for the noise case.

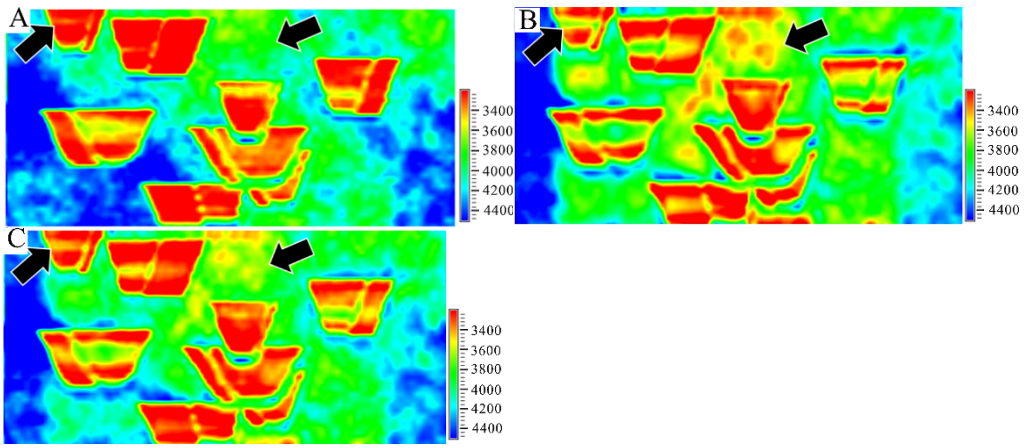


Figure 10. Stanford reservoir model and inversion comparison. (A) Sand-body velocity model. (B) Conventional facies-constrained inversion. (C) Multi-level facies-constrained inversion.

facies priors for complex sand-body prediction, while the conclusion remains limited to model-space validation.

Fourteen pseudo-wells were extracted from the inverted 3D model for quantitative comparison (Figure 11). The conventional method matched 11 of the 14 pseudo-wells, whereas the proposed method matched 13 of the 14 pseudo-wells. The agreement rate therefore increased from 78.57% to 92.86%. This metric is a facies-agreement measure in the synthetic model, not a blind-field accuracy metric.

Figure 12 and Table 2 present the planar inversion results and the facies-agreement analysis, respectively. Planar slices were further examined to test lateral sand-body recovery. The conventional method tends to blur boundaries and locally loses narrow sand bodies, whereas the proposed method better preserves the geometry of the channelized low-velocity bodies. Sensitivity tests indicate that the method is sensitive to the quality of the facies prior and to noise in weak-reflection intervals. Therefore, uncertain areas far from Well A1 should be interpreted conservatively.

4. Field application: Multi-attribute fusion and sweet-spot prediction

After the validation tests, the workflow was applied to the Baodao northern slope field data. The aim of the

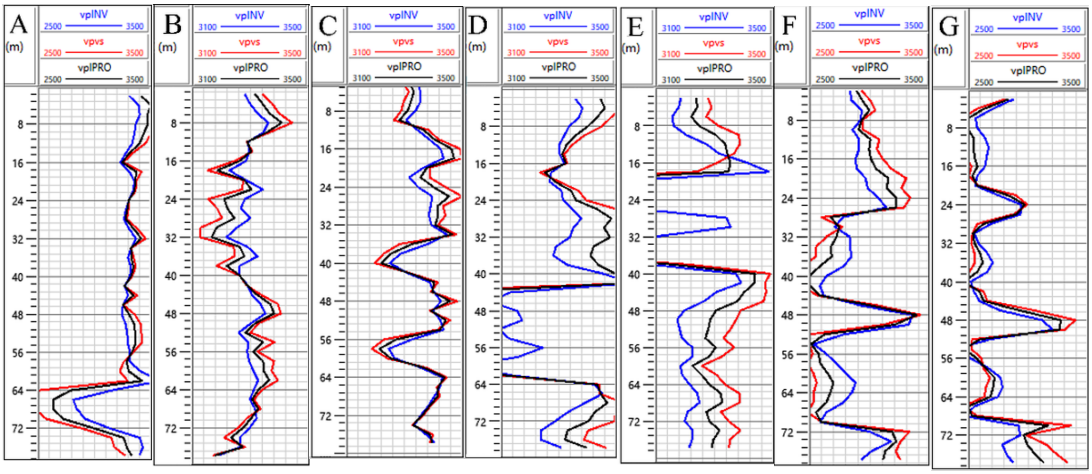


Figure 11. Pseudo-well comparison of inversion curves. Panels A–G correspond to pseudo-wells A, B, C, D, E, F, and G, respectively. In each panel, the red curve denotes the true model, the blue curve denotes the conventional facies-constrained inversion, and the black curve denotes the proposed multi-level facies-constrained inversion.

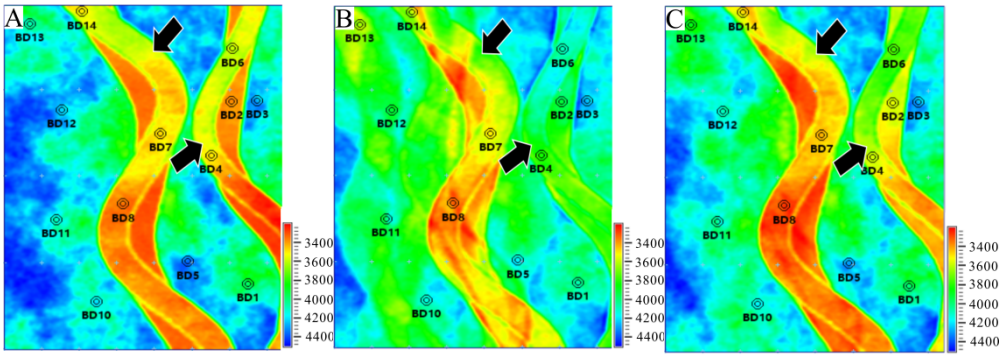


Figure 12. Planar inversion results for the Stanford model. (A) True model. (B) Conventional facies-constrained inversion. (C) Proposed multi-level facies-constrained inversion.

field application was to rank favorable reservoir zones by integrating elastic, petrophysical, and gas-sensitive attributes. Because independent blind-well validation was unavailable, the resulting maps were reported as probabilistic sweet-spot predictions and were interpreted together with geological plausibility and A1 calibration.

4.1. Semi-supervised deep learning for porosity prediction

Porosity prediction was performed using a semi-supervised bidirectional long short-term memory model. Labeled samples were constructed by time-depth matching the porosity log of Well A1 to the co-located seismic traces within the interpreted target interval. Unlabeled samples were extracted from seismic traces in the same stratigraphic interval away from the well. The sequential seismic-attribute vectors were normalized using statistics calculated from the labeled training interval, and the same transformation was applied to validation and unlabeled samples. This separation prevents information from the validation blocks from entering the preprocessing statistics.

The operational sequence was as follows: (i) labeled and unlabeled depth-ordered sequences were constructed; (ii) the preprocessing transformation was fitted only on the labeled training blocks; (iii) the supervised and consistency terms were jointly trained; (iv) the training state was selected using blocked validation and early stopping; (v) the trained network was applied trace by trace; and (vi) predictions that were far from calibration or inconsistent with the facies prior were masked or down-weighted. All four sand-body predictions used the same trained architecture and decision rules.

The bidirectional long short-term memory architecture

contains two bidirectional recurrent layers with 64 and 32 hidden units, followed by an attention layer and a fully connected output layer. Dropout was 0.20. Training minimized a weighted combination of the supervised porosity-prediction error at Well A1 and a consistency penalty between predictions from the original and perturbed versions of each unlabeled seismic sequence. The consistency weight was selected from the blocked validation intervals and was then held fixed during prediction. Adam was used with an initial learning rate of 1×10^{-3}, a maximum of 200 epochs, and early stopping after 20 epochs without improvement in validation loss. ReLU, tanh, and Mish were compared under the same blocked validation scheme; tanh was retained because it provided the most stable convergence. Depth-contiguous blocks, rather than randomly mixed samples, were used for validation to reduce leakage caused by vertical autocorrelation. Because only one field well was available, uncertainty was assessed from validation residuals, distance from Well A1, and consistency with the coupled facies prior; the resulting porosity volume was therefore interpreted as a relative prediction rather than as blind-well-validated absolute porosity.

Table 2. Facies-agreement analysis of different facies-constrained inversion methods in the Stanford model test

Pseudo-well	Conventional facies-constrained inversion	Multi-level facies-constrained inversion
BD1	Match	Match
BD2	No match	Match
BD3	Match	Match
BD4	Match	Match
BD5	Match	Match
BD6	No match	No match
BD7	Match	Match
BD8	Match	Match
BD9	Match	Match
BD10	Match	Match
BD11	Match	Match
BD12	No match	Match
BD13	Match	Match
BD14	Match	Match
Match probability	78.57%	92.86%

The input features included five pre-stack inversion attributes: P-impedance, S-impedance, density, P/S velocity ratio, and lambda-rho. A total of 1,268 labeled samples were extracted from Well A1 within the target interval, and 5,200 unlabeled samples were collected from seismic traces in the same interval. The dataset was divided into training (70%), validation (15%), and test (15%) sets by stratigraphic blocks to prevent vertical leakage. The mean absolute error on the test set was 1.2%, and the correlation coefficient R was 0.89.

The predicted porosity slices are shown in Figure 13. The 3U-A and 3L-B sand bodies showed relatively continuous favorable porosity zones, with average porosities of 8.3% and 8.1%, respectively. The 3U-B and 3L-A sand bodies contained local high-porosity zones with maximum porosities of 15.7% and 16.3%, respectively. Because the calibration was based on a single well, the porosity map should be used as a relative distribution indicator. Areas far from Well A1 or inconsistent with sedimentary facies were assigned lower confidence.

4.2. Prediction of hydrocarbon potential using frequency-dependent amplitude variation with offset and relative flowability attributes

Conventional post-stack fluid indicators do not fully use angle-dependent pre-stack information. Therefore, this study extracted a relative flowability attribute from frequency-dependent AVO responses. The attribute was used as a gas-sensitive indicator rather than an absolute permeability measurement.

The relative-flowability workflow was applied to the PP pre-stack angle gathers in seven operations: (i) amplitude-preserving quality control and angle-gather alignment were performed; (ii) strong background reflections were separated by waveform decomposition; (iii) the weak reservoir-response component were constructed; (iv) fast Fourier transform spectra was used to retain the frequency interval with stable energy and consistent well-tie behavior, and the 8–35 Hz frequency band was selected; (v) localized angle-dependent spectra was calculated with the generalized S-transform; (vi) spectral balancing was applied and each component was normalized to [0, 1]; and (vii) the normalized frequency-dependent AVO terms were combined using **Equation 20**. The weights were calibrated at Well A1 to agree with the log-interpreted reservoir interval and were then kept unchanged for all four sand bodies. This fixed-parameter application reduces the risk of tuning each target map independently. The relative flowability attribute is expressed as **Equation 17**.

Relative flowability was used here as an interpretive name for a normalized seismic attribute, not as a direct estimate of Darcy-scale mobility. The calculation was

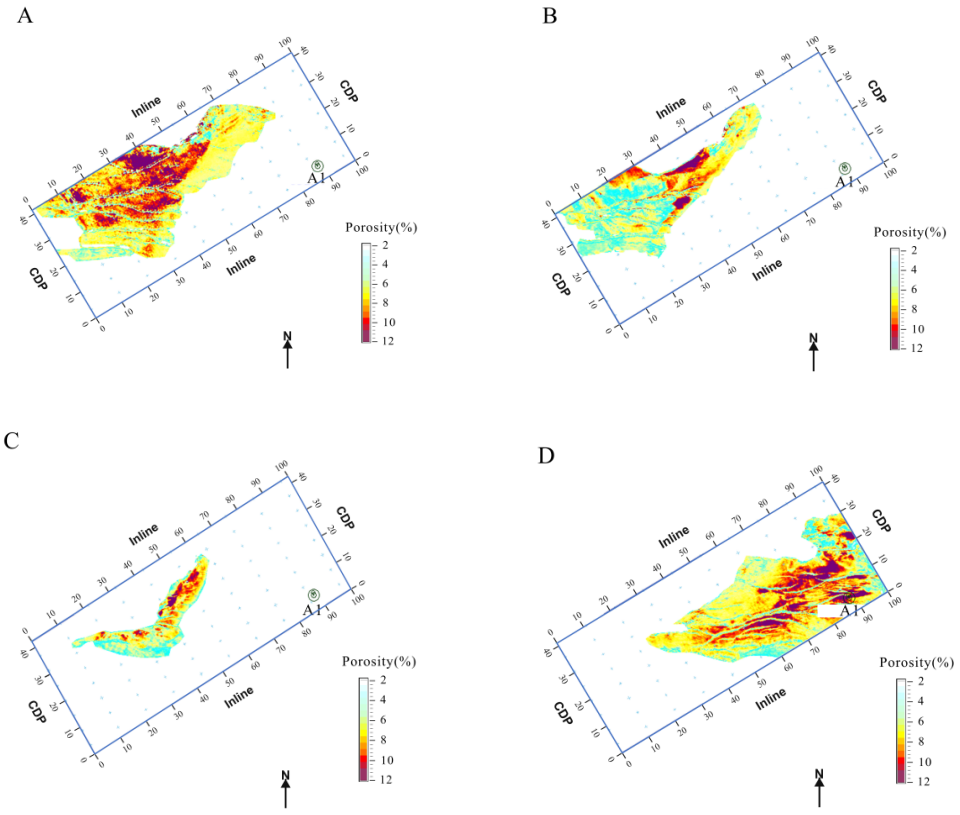


Figure 13. Predicted porosity slices for the target sand bodies. (A) 3U-A. (B) 3L-A. (C) 3U-B. (D) 3L-B. Values are interpreted as relative porosity predictions calibrated by Well A1.

performed after the inversion and porosity steps so that an anomaly was retained as favorable only when its spectral AVO response, elastic response, porosity prediction, and facies prior were mutually consistent.

$$F_r(f,\theta) = N\left\{\frac{|A(f,\theta)|}{f}\right\} \tag{17}$$

where F_r is the normalized relative flowability attribute, $A(f, \theta)$ is the instantaneous amplitude spectrum at frequency f and incidence angle θ, and $N\{\}$ denotes normalization to [0, 1]. The frequency-dependent AVO response is written as **Equations 18–20**:

$$R(\theta,f) = \frac{A(f,\theta)}{A_0(f)} \tag{18}$$

$$A_0(f) = mean_\theta A(f,\theta) \tag{19}$$

$$G_h = w_1 F_r + w_2 R(\theta,f) \tag{20}$$

where the normalized frequency-dependent reflection response represents the angle-dependent spectral anomaly, the angle-averaged spectrum represents the background spectral level, and the gas-sensitive indicator combines their calibrated contrast. The weighting coefficients were constrained using Well A1 and applied unchanged throughout the mapped interval. The workflow returns a dimensionless relative indicator: it ranks anomalies within the study area.

Applying **Equation 20** yields the gas-sensitive attribute maps in Figures 14 and 15. The 3U-A sand body showed the strongest gas-sensitive response in the southwestern part of the study area, while the 3L-B sand body showed a relatively strong response in the eastern part. The 3U-B and 3L-A sand bodies showed weaker and more discontinuous anomalies. These results were used only where they agreed with facies-constrained inversion and porosity prediction.

4.3. Multi-attribute fusion based on competitive neural networks

The final sweet-spot prediction integrated the P/S velocity ratio, predicted porosity, and gas-sensitive attributes. These

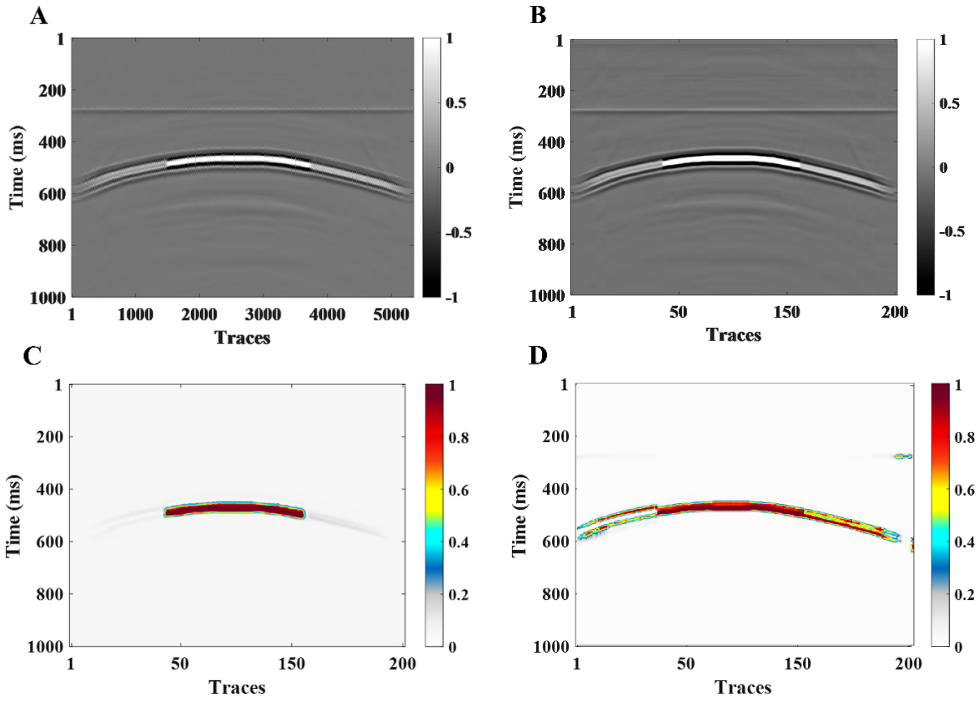


Figure 14. Forward-model and gas-sensitive attribute comparison. (A) Pre-stack gather from wave-equation forward modeling. (B) Post-stack section. (C) Pre-stack frequency-dependent amplitude variation with offset gas-sensitive result. (D) Conventional post-stack hydrocarbon indicator.

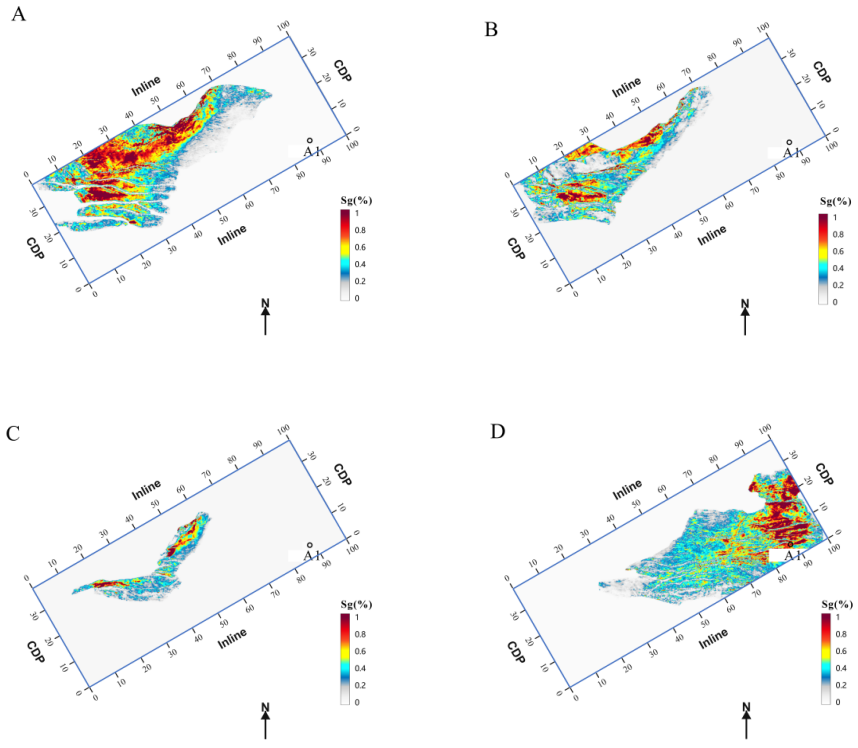


Figure 15. Gas-sensitive attribute slices for the four sand bodies. (A) 3U-A. (B) 3U-B. (C) 3L-A. (D) 3L-B. Warmer colors indicate stronger relative gas-sensitive response.

attributes represent elastic response, storage capacity, and fluid sensitivity, respectively. Before fusion, each attribute was normalized, and low-confidence areas were down-weighted according to distance from calibration, facies inconsistency, and low seismic-data quality.

The fusion procedure contains four steps: (i) reservoir-sensitive attributes that are physically complementary and consistent with Well A1 were selected; (ii) the attributes were normalized and weighted according to their calibration consistency; (iii) redundancy was reduced with PCA; and (iv) the fused feature space was classified with a competitive neural network. Class I favorable zones represent areas where low P/S velocity ratio, relatively high porosity, and strong gas-sensitive response were mutually consistent. Class II zones satisfied only part of these conditions. Non-favorable zones lacked consistent reservoir or gas-sensitive evidence.

The comprehensive prediction results are shown in Figure 16. The Class I favorable zone of 3U-A covered 18 km^2, and the combined Class I and Class II area was 83 km^2. The Class I favorable zone of 3U-B covered 16 km2, with 38 km^2 for Class I and Class II combined. The 3L-A sand body had a smaller Class I area of 6 km^2 and a combined favorable area of 15 km^2. The 3L-B sand body had the largest favorable area, with 41 km^2 of Class I zones and 113 km^2 of Class I plus Class II zones. These areas should be regarded as ranked exploration targets pending future drilling verification.

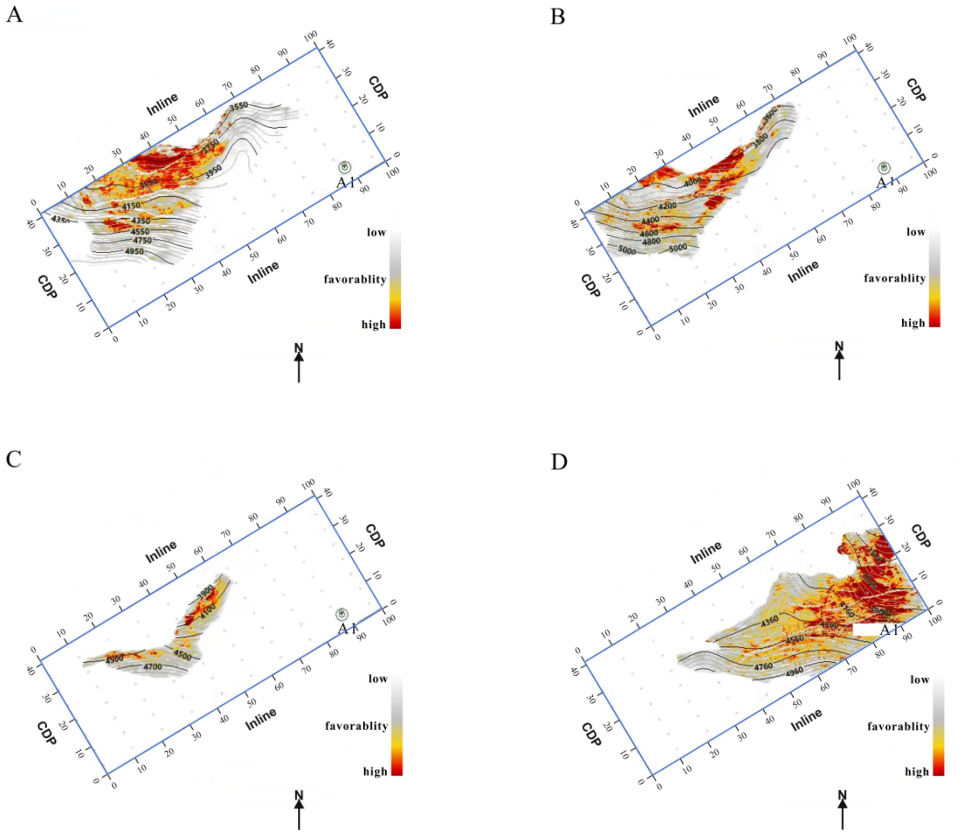


Figure 16. Comprehensive sweet-spot prediction results. (A) 3U-A. (B) 3U-B. (C) 3L-A. (D) 3L-B. Brown indicates Class I favorable zones, yellow indicates Class II favorable zones, and other colors indicate non-favorable or lower-confidence zones.

5. Conclusion

This study developed and tested a multi-level facies-constrained reservoir prediction workflow for sparse-well deepwater exploration in the northern slope of the Baodao Sag, Qiongdongnan Basin. The workflow integrated sedimentary facies, seismic waveform facies, logging lithofacies, Bayesian exact Zoeppritz inversion, semi-supervised porosity prediction, frequency-dependent AVO analysis, and competitive neural network attribute

fusion.

The main methodological contribution was the coupled facies-prior model. Rather than using a single facies constraint or an arbitrary linear attribute stack, the proposed workflow linked sedimentary interpretation, seismic waveform clustering, and log-interpreted lithofacies into a probability-based prior for inversion and reservoir evaluation.

The competitive neural network achieved the highest lithofacies agreement at the calibration well among the tested clustering methods, with agreement rates of 71.4% for FCM, 80.3% for SOM, and 86.6% for the competitive neural network. This comparison supports the use of competitive learning for nonlinear facies fusion, although the result should be interpreted as calibration-well evidence rather than blind-field validation.

Synthetic tests and the Stanford model test indicate that the proposed inversion better preserved weak reflection information and sand-body boundaries than the conventional facies-constrained workflow. In the Stanford model, facies agreement increased from 78.57% to 92.86%. This result demonstrates algorithmic stability in model tests, but independent field validation still requires future drilling or additional wells.

The field application delineates Class I and Class II favorable zones in the four target sand bodies. Among them, 3L-B had the largest combined favorable area of 113 km^2 and the most continuous favorable distribution. These predictions provide a geological basis for exploration deployment.

Overall, the workflow offers a practical route for integrating limited well control with pre-stack seismic information in deepwater sparse-well areas. Its broader application should be accompanied by local rock-physics calibration, uncertainty analysis, and validation by new wells whenever available.

Acknowledgments

None.

Funding

None.

Conflict of interest

The authors declare no potential conflict of interest.

Author contributions

Conceptualization: Wanyuan Sun
Formal analysis: Rui Wang
Investigation: Rui Wang
Methodology: Shiyou Liu
Writing–original draft: Shuxian Liu
Writing–review & editing: Shuxian Liu

Availability of data

All data analyzed have been presented in the paper.

References

1. Chen P, Lu Y, Wang Z, Chen L. Seismic image prediction of Cenozoic reef-banks in the northwestern South China Sea. *J Earth Sci*. 2012;23(4):597-611.

   doi: 10.1007/s12583-012-0277-y

2. Feng Y, Ren Y, Li Z, Jin L. Geological interpretation and hydrocarbon exploration potential of three types of mound-shaped reflectors in the Meishan Formation, southern Qiongdongnan Basin. *Acta Geol Sin (Engl)*. 2021;95(1):167-176.

   doi: 10.1111/1755-6724.14636

3. Pacheco JMÚ, Bayón PV, Correia U, Kneller E, Peiro M. Unlocking the properties of a presalt carbonate reservoir offshore Brazil with facies-constrained geostatistical inversion. *Lead Edge*. 2022;41(12):832-839.

   doi: 10.1190/tle41120832.1

4. Xie Q, Wu Y, Huang Q, *et al*. Prediction of marine thin shale gas reservoir with seismic phase-controlled nonlinear stochastic inversion. *Processes*. 2023;11(8):2301.

   doi: 10.3390/pr11082301

5. Zheng C, Zhang B, Li R, *et al*. Facies-controlled prediction of dolomite reservoirs in the Middle Permian Qixia Formation in Shuangyushi, northwestern Sichuan Basin. *Energy Geosci*. 2024;5(2):100230.

   doi: 10.1016/j.engeos.2023.100230

6. Su Q, Xu X, Chen T, Zong J, Wang H. A facies-constrained geostatistical seismic inversion method based on multi-scale sparse representation. *Geophys Prospect*. 2024;72(5):1657-1671.

   doi: 10.1111/1365-2478.13476

7. Fernandes FJD, Teixeira L, Freire AFM, Lupinacci WM. Stochastic seismic inversion and Bayesian facies classification applied to porosity modeling and igneous rock identification. *Pet Sci*. 2024;21(2):918-935.

   doi: 10.1016/j.petsci.2023.11.020

8. Zhang H, Chen L, Zhu H, Xin Y, Wang Y, Sun X. Prediction of marl reservoir distribution based on facies-constrained reflectivity inversion method. *Front Earth Sci*. 2024;12:1495720.

   doi: 10.3389/feart.2024.1495720

9. Caers J, Hoffman T. The probability perturbation method: a new look at Bayesian inverse modeling. *Math Geol*. 2006;38(1):81-100.

doi: 10.1007/s11004-005-9005-9

10. Huang Y, Xu LH, Yang HD, He QL, He YH, Yang QJ. Fanyan yueshu de duodian dizhi tongjixue jianmo—yi Daqing changyuan luxiang youtian weili [Multi-point geostatistical modeling with inversion constraints: A case study of continental oil fields in Daqing placanticline]. *Oil Geophys Prospect*. 2022;57(6):1445-1452. [In Chinese].

doi: 10.13810/j.cnki.issn.1000-7210.2022.06.020

11. Bosch M, Mukerji T, Gonzalez EF. Seismic inversion for reservoir properties combining statistical rock physics and geostatistics: a review. *Geophysics*. 2010;75(5):75A165-75A176.

doi: 10.1190/1.3478209

12. Buland A, Omre H. Bayesian linearized AVO inversion. *Geophysics*. 2003;68(1):185-198.

doi: 10.1190/1.1543206

13. Chen H, Han J, Li K. Facies-constrained simultaneous inversion for elastic parameters and fracture weaknesses using azimuthal partially incidence-angle-stacked seismic data. *Geophys Prospect*. 2024;73(2):562-574.

doi: 10.1111/1365-2478.13659

14. Larsen AL, Ulvmoen M, Omre H, Buland A. Bayesian lithology/fluid prediction and simulation on the basis of a Markov-chain prior model. *Geophysics*. 2006;71(5):R69-R78.

doi: 10.1190/1.2245469

15. Liu M, Jervis M, Li W, Nivlet P. Seismic facies classification using supervised convolutional neural networks and semisupervised generative adversarial networks. *Geophysics*. 2020;85(4):O47-O58.

doi: 10.1190/geo2019-0627.1

16. Cai H, Wu Q, Ren H, *et al*. Pre-stack texture-based semi-supervised seismic facies analysis using global optimization. *J Seism Explor*. 2019;28(6):513-532.

17. Zhao M, Wang YQ, Peng ZM, *et al*. Seismic multi-attribute fusion using fast independent component analysis and its application. *J Seism Explor*. 2019;28(1):89-101.

18. Song Z, Li S, He S, Yuan S, Wang S. Gas-bearing prediction of tight sandstone reservoir using semi-supervised learning and transfer learning. *IEEE Geosci Remote Sens Lett*. 2022;19:1-5.

doi: 10.1109/LGRS.2022.3177314

19. Dhara A, Sen MK, Biswas R. Facies-constrained transdimensional amplitude versus angle inversion using machine learning assisted priors. *Geophys Prospect*. 2023;71(4):590-613.

doi: 10.1111/1365-2478.13339

20. Xie Y, Zhang G, Tang W, Zhao Z. TNanhai beibu shenshuiqu youqi chengcang lilun jishu chuangxin yu kantan zhongda tupo [Theoretical and technological innovation of oil and gas accumulation and major exploration breakthroughs in deep-water areas, northern South China Sea]. *Nat Gas Ind*. 2020;40(12):1-11. [In Chinese].

doi: 10.3787/j.issn.1000-0976.2020.12.001

21. Xie Y, Gao Y. Zhongguo haiyou jinqi guonei kantan jinzhan yu kantan fangxiang [Recent domestic exploration progress and direction of CNOOC]. *China Pet Explor*. 2020;25(1):20-30. [In Chinese].

doi: 10.3969/j.issn.1672-7703.2020.01.003

22. Xie YH. FJiyu dizhen gouxiang de xiangkong chuceng yuce fangfa [Facies-controlled reservoir prediction based on the seismic configuration]. *Geophys Prospect Pet*. 2021;60(5):784-793. [In Chinese].

doi: 10.3969/j.issn.1000-1441.2021.05.009

23. Fu C, Xie Y, Song L, *et al*. Jiyu chenji moni de xuni jing jianli yu shenshui xiagu xiangkong jianmo celue—yi Qiongdongnan pendi zhongyang xiagu Lingshui duan weili [Pseudo-well setting and strategy of facies-controlled reservoir modeling of deep water canyon based on sedimentary simulation: Taking the Lingshui section of the Central Canyon in Qiongdongnan Basin as an example]. *Mar Orig Pet Geol*. 2023;28(4):413-424. [In Chinese]. Accessed November 3, 2026. https://www.hxyqdz.com/CN/Y2023/V28/I4/413

24. Yin X, Liu C, Wang B. Jiyu hunhe yichuan suanfa de dieqian suiji fanyan fangfa [Pre-stack stochastic inversion based on hybrid genetic algorithm]. *J China Univ Pet (Ed Nat Sci)*. 2017;41(4):57-64. [In Chinese].

doi: 10.3969/j.issn.1673-5005.2017.04.008

25. Yin X, Kong S, Zhang F, Zhang X. Jiyu chayi yanhua suanfa de dieqian AVO fanyan [Pre-stack AVO inversion based on the differential evolution algorithm]. *Oil Geophys Prospect*. 2013;48(6):948-953. [In Chinese].

doi: 10.13810/j.cnki.issn.1000-7210.2013.04.013

26. Liang J, Wang Q, Hao L, Tang J, Liao P. Chengyanxiang fenxi fangfa zai Nanhai beibu shenshuiqu chuceng yuce de yingyong—yi Zhujiangkou pendi Baiyun aoaxian weili [Application of diagenetic facies analysis to reservoir prediction in deep water area of the northern South China Sea: A case study from Baiyun Sag, Zhujiangkou Basin]. *Acta Sedimentol Sin*. 2011;29(3):503-512. [In Chinese].

doi: 10.14027/j.cnki.cjxb.2011.03.002

27. Yin X, Zhang S, Zhang F, *et al*. Liyong jiyu Russell jinsi de tanxing bozu kang fanyan jinxing chuceng miaoshu he liuti shibie [Utilizing Russell approximation-based elastic wave impedance inversion to conduct reservoir description and fluid identification]. *Oil Geophys Prospect*. 2010;45(3):373-380. [In Chinese]. Accessed November 3, 2026. http://www.

ogp-cn.com.cn/EN/Y2010/V45/I3/373

28. Gu W, Yin X, Wu F, Li K, Zhai H. Boxing qudong xia duocanshu yueshu gao fenbianlv fanyan fangfa—yi Sichuan pendi Yuxi diqu Longmaxi zu yeyanqi weili [Multi-parameter constrained high-resolution inversion method driven by waveform: A case study of Longmaxi Formation shale gas in western Chongqing, Sichuan Basin]. *Oil Geophys Prospect*. 2021;56(6):1311-1321. [In Chinese].

    doi: 10.13810/j.cnki.issn.1000-7210.2021.06.014

29. Ling T, You L, Lu Y, Luo W, Ye Q. Qiongdongnan pendi Baodao aoaxian nan xiepo haidishan chenji tezheng yu youli chuceng yuce [Sedimentary characteristics and high-quality reservoir prediction of submarine fan in the southern continental slope of Baodao Sag, Qiongdongnan Basin]. *Complex Hydrocarbon Reserv*. 2025;18(3):311-317. [In Chinese].

    doi: 10.16181/j.cnki.fzyqc.2025.03.008

30. Xu X, Zhou W, Zhang C, *et al*. Shenshui shenceng di shen youqi cang chuceng tezheng ji wuxing kongzhi yinsu—yi Qiongdongnan pendi Baodao aoaxian nan po Lingsan duan weili [Reservoir characteristics and physical property control factors in deep water and low-permeability oil and gas reservoirs: A case study of the 3rd member of Lingshui Formation on the southern slope of Baodao Sag in Qiongdongnan Basin]. *Mar Orig Pet Geol*. 2026;31(1):48-60. [In Chinese].

    doi: 10.3969/j.issn.1672-9854.2026.01.004

31. Xu C, You L. North slope transition zone of Songnan-Baodao sag in Qiongdongnan Basin and its control on medium and large gas fields, South China Sea. *Pet Explor Dev*. 2022;49(6):1229-1242.

    doi: 10.1016/S1876-3804(23)60345-3

32. Park DC. Centroid neural network for unsupervised competitive learning. *IEEE Trans Neural Netw*. 2000;11(2):520-528.

    doi: 10.1109/72.839021

33. Park DC, Kwon OH, Jeon BN. Centroid neural network with a divergence measure for GPDF data clustering. *IEEE Trans Neural Netw*. 2008;19(6):948-957.

    doi: 10.1109/TNN.2007.2000051